Cytoglobin regulates ventricular morphogenesis and diastolic function through sGC-cGMP signaling during development.

Adam Austin Clark[1], Rasmus Hejlesen[3], Tzu-Ting, Weng[1], Muddassar Iqbal[2], Akueba Bruce[2], Paola Corti[1#]

[1]Department of Biochemistry and Molecular Biology, University of Maryland School of Medicine, Baltimore, MD 21201

[2]Department of Medicine, University of Maryland School of Medicine, Baltimore, MD 21201

[3]MRC Human Genetics Unit, Institute of Genetics and Cancer, The University of Edinburgh, Edinburgh, EH4 2XU, UK

#Correspondence: Corti, Paola. Email: PCorti@som.umaryland.edu

Abstract

Aims. Hypoplastic left heart syndrome (HLHS) is a severe congenital heart disease characterized by ventricular hypoplasia and impaired cardiac function. Clinically, inhaled nitric oxide (NO) therapy is used to reduce pulmonary vascular resistance and improve cardiopulmonary stability in HLHS patients. However, whether NO signaling contributes to HLHS pathogenesis remains unknown. Cytoglobin (CYGB) is a heme protein traditionally thought to limit NO bioavailability. Unexpectedly, our recent work shows that CYGB/Cygb enhances NO signaling through activation of the nitric oxide synthase- soluble guanylate cyclase (sGC)- cyclic guanosine monophosphate (cGMP) signaling pathway. In zebrafish embryos, Cygb-dependent NO signaling is required for normal cilia motility and for the establishment of correct cardiac laterality. Here, our aim was to determine whether Cygb-dependent NO-sGC signaling linked to cilia function regulates cardiac morphogenesis and contributes to ventricular hypoplasia in HLHS.

Methods and Results. We found that loss of *Cygb* (*cygb2*) in zebrafish disrupts NO-sGC signaling during cardiogenesis, altering cardiac progenitor organization and migration within the anterior lateral plate mesoderm (ALPM). Disruption of these processes impairs heart tube morphogenesis, thereby producing a compact ventricle with increased wall thickness despite preserved cardiomyocyte number, reduced ventricle size and decreased stroke volume, recapitulating key features of HLHS. Genetic disruption of the sGC α-subunit (*gucy1a1)* and pharmacological NO scavenging phenocopy the *cygb2* mutant phenotype, resulting in reduced cGMP levels, compact ventricular architecture and decreased stroke volume (SV). Consistently, restoration of NO-sGC signaling in *cygb2* mutants rescues early cardiac progenitor patterning, ventricular morphology and SV.

Conclusions. These findings identify Cygb-dependent NO-sGC signaling as a critical developmental pathway for ventricular development and performance, temporally linking cardiac progenitor dynamics to cilia-dependent signaling associated with left-right patterning. This study further suggests that pharmacological activation of sGC may provide a therapeutic strategy for hypoplastic ventricular disease.

Keywords: Hypoplastic left heart syndrome, soluble guanylyl cyclase, nitric oxide, cardiac development, zebrafish.

50 **Graphical Abstract**

51

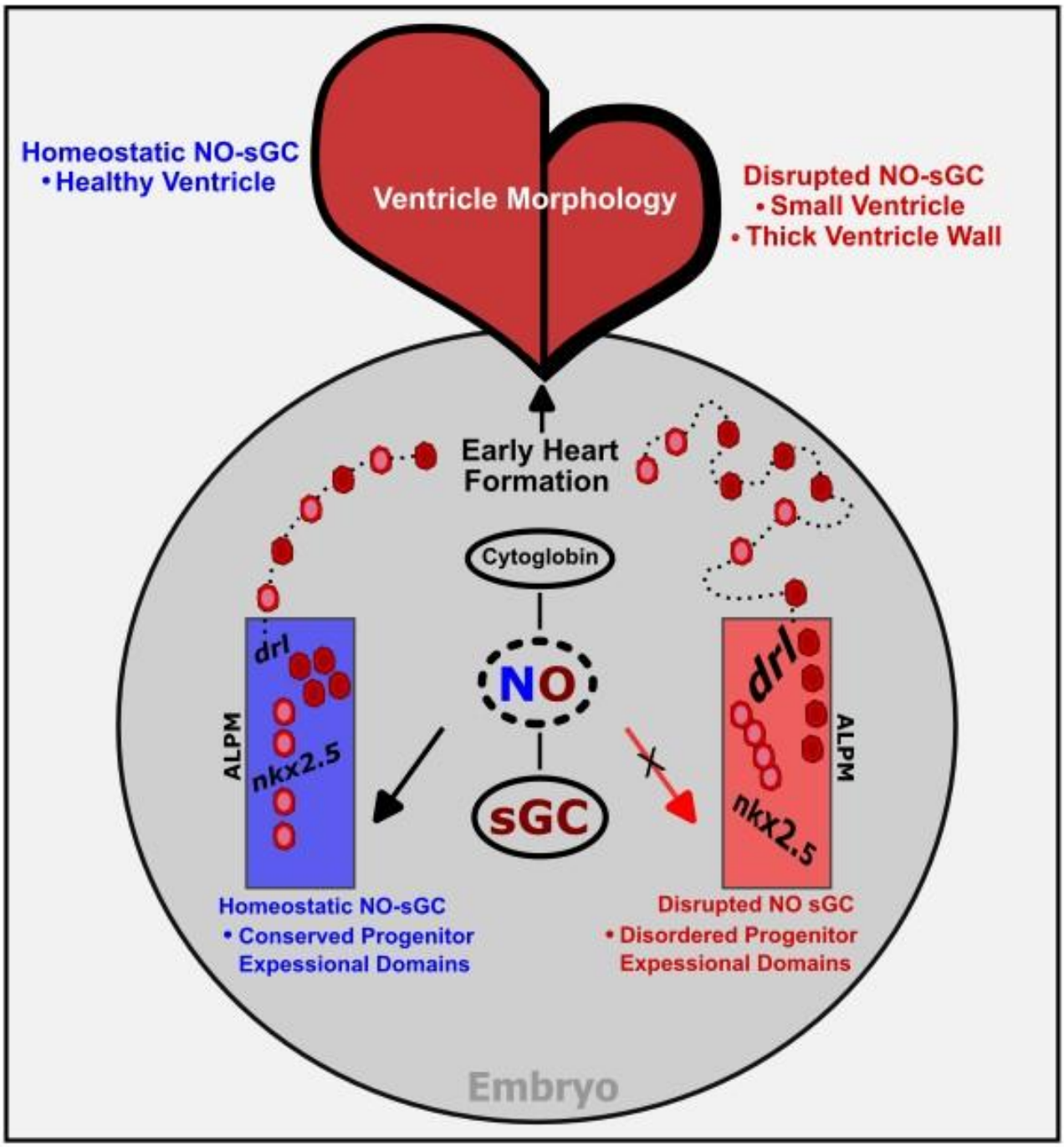

52

53

54

55

1. Introduction

Hypoplastic left heart syndrome (HLHS) is a complex congenital heart disease (CHD) with a multigenic etiology.[1,2] Familial clustering supports a genetic basis, yet the majority of causative genes remain unidentified. The phenotype is heterogeneous, variably affecting the left ventricle, valves, and aortic outflow tract, and no single-gene mutation has been shown to reproduce the full HLHS spectrum in animal models. Traditionally, HLHS was attributed to diminished intracardiac flow during development, leading to secondary hypoplasia. However, recent work has shifted this paradigm, suggesting that HLHS may arise from primary defects in myocardial and endocardial development, resembling a developmental cardiomyopathy in origin rather than a purely hemodynamic lesion.[3] Additionally, an emerging body of evidence links HLHS to disturbances of left–right (LR) patterning and cilia function, suggesting a new developmental mechanism contributing to disease pathogenesis.[4] Based on case reports and large registry-based analyses.[4,5] HLHS has been observed in association with heterotaxy, situs inversus, gut malrotation, biliary atresia and splenic anomalies.[6-8] These observations further support the concept that defects in laterality determination and ventricular morphogenesis may share developmental origins. According to recent interpretations, HLHS may originate from early intrinsic disruptions in cardiac progenitors arising during and prior to heart tube formation, and may occur in parallel with, or as a consequence of, abnormal left-right signaling.[9] Findings from recessive forward genetic screens in fetal mice further support this view, revealing that cilia and cilia-transduced signaling pathways play central roles in HLHS pathogenesis.[10]

Integrative genetic analysis combining human sequencing with developmental datasets and mouse models of HLHS identified CYGB as a candidate gene within a developmental gene network associated with the disease,[11] suggesting a potential role for CYGB in pathways regulating early cardiac morphogenesis. CYGB is a hexa-coordinate heme-containing globin expressed ubiquitously in vertebrate tissues.[12,13] Unlike its penta-coordinate relatives, hemoglobin and myoglobin, which primarily

81 bind and transport oxygen, CYGB is more prone to function as a redox-active enzyme regulating NO
82 metabolism through reversible redox cycling of its heme iron.[14] The reduced heme iron can catalyze
83 nitrite reduction to bioactive NO,[13,15] while the oxygenated heme iron can dioxygenate NO to inert
84 nitrate,[16-18] thus maintaining oxygen-dependent NO homeostasis. While these reactions are possible
85 in vitro, mouse studies indicate that the predominant physiological role of CYGB is to scavenge NO,
86 modulating vascular tone through NO deoxygenation[19] and to protect cells against oxidative stress via
87 superoxide dismutase-like activity.[20] Unexpectedly, we discovered a new critical role for Cygb in
88 development, where CYGB/Cygb instead enhances NO signaling through activation of the nitric oxide
89 synthase- sGC-cGMP signaling pathway.[21] The zebrafish *cygb2* knockout exhibits cardiac laterality
90 defects due to impaired NO signaling, a phenotype characteristic of human disorders associated with
91 defective cilia function. Mechanistically we demonstrated that Cygb2 localizes to cilia within the
92 Kupffer's vesicle (KV), the zebrafish laterality organ. Loss of *cygb2* disrupts ciliary structure, motility
93 and directional fluid flow, resulting in impaired KV activity and cardiac laterality defects.[21] Whether this
94 function is directly linked to cardiac morphogenesis mimicking HLHS remains unknown and the extent
95 to which Cygb dependent regulation of laterality intersects, potentially through ciliary mechanisms, has
96 not been explored.
97
98 Zebrafish cardiac development initiates within the ALPM, where bilateral populations of mesodermal
99 progenitors undergo progressive spatial organization prior to overt myocardial differentiation.[22,23]
100 Between the 14–16 somite stages (ss), these progenitors undergo tightly coordinated mediolateral
101 convergence and anterior–posterior elongation to assemble a coherent cardiac disc that
102 subsequently transforms into the linear heart tube.[23,24] Ventricular formation is exquisitely sensitive to
103 perturbations in progenitor number and spatial positioning as even subtle defects in coordinated cell
104 migration or tissue architecture can give rise to small, compact ventricles, whereas atrial development
105 may remain relatively preserved due to reliance on progenitor contributions from populations residing

106 in spatially segregated domains regulated by alternative signaling ques .[24,25] Importantly,
107 morphogenetic events critical to ventricular development occur immediately downstream of KV
108 mediated left–right axis establishment,[23,26] raising the possibility that laterality patterning cues
109 coordinating embryonic asymmetry also influence spatial patterning and migratory behavior of cardiac
110 progenitors, shaping ventricular growth and chamber morphogenesis. One of the earliest markers of
111 cardiac progenitors in zebrafish is *draculin* (*drl*), a transcription factor activated during gastrulation
112 that delineates bilateral cardiac progenitor fields within the ALPM.[23,27] During somitogenesis tracking
113 *drl* expression marks cardiac progenitor organization and collective migratory behavior. Within the
114 ALPM alterations in spatial geometry such as anterior–posterior elongation of the *drl* domain reflects
115 early disruption of progenitor spatial patterning,[23] defects expected to impair migratory ques and
116 ventricle assembly. Thus, alterations in *drl* expression may represent one of the earliest
117 developmental events that ultimately lead to hypoplastic ventricular growth. As development
118 proceeds, myocardial *drl* expression is restricted to first heart field descendants, providing a readout
119 of cardiac disc formation and heart tube assembly, stages that directly precede ventricular chamber
120 growth and functional maturation.[22]
121
122 *NKX2 homeobox 5* (*Nkx2.5)* encodes a conserved cardiac homeobox transcription factor expressed
123 within the forming cardiac disc at the transition from migratory cardiac progenitors to differentiated
124 myocardium.[23,27] In both mouse models and human patients, dysregulation of NKX2.5 activity is
125 associated with congenital heart diseases and hypoplastic ventricular phenotypes[28]. In the zebrafish
126 embryo, *nkx2.5* expression is conserved and is initially induced in bilateral ALPM domains as cardiac
127 progenitors converge toward the midline, coinciding with progenitor stabilization and the initiation of
128 chamber-specific transcriptional programs.[29] By 28 hpf, *nkx2.5* expression marks specified
129 cardiomyocytes within the heart tube, predominantly ventricular myocardium,[24] such that its expression
130 at this stage reflects proper myocardial differentiation and maintenance of cardiac identity.

131 While Cygb-dependent regulation of embryonic laterality is now established,[21] its role in coordinating
132 cardiac progenitor migration and myocardial differentiation remains unknown. Here, we demonstrate
133 that *cygb2* deficiency in zebrafish disrupts early cardiac progenitor organization and ventricular
134 chamber formation, producing a small, compact ventricle with reduced diastolic filling. These features
135 parallel ventricular hypoplasia and impaired compliance observed in HLHS. Crucially, these defects are
136 phenocopied in sGC mutants and fully rescued by pharmacological activation of NO-sGC signaling,
137 identifying a developmental pathway that links ciliary NO regulation to cardiac progenitor
138 morphogenesis and ventricular growth.
139

140 **2. Methods**

141 All animal studies were approved by the University of Maryland Institutional Animal Care and Use
142 Committee (IACUC-1022015), Baltimore, MD, USA. The programs and facilities are USDA registered
143 and covered under an assurance with the Office of Lab Animal Welfare (OLAW). Procedures followed
144 guidelines outlined by the NIH Guide for the Care and Use of Laboratory Animals (8th Edition, 2011).
145 Embryos were maintained at 28.5 °C until the desired developmental stage. Animals were euthanized
146 according to approved protocols; embryos >3 days post fertilization (dpf) to adult (anesthetic overdose
147 300mg/L buffered tricane), embryos <3dpf (paraformaldehyde immersion).
148

149 **2.1 Animal Studies**

150 For all experiments, clutch-matched embryos from dome stage (~ 4hpf) to 5dpf were randomly assigned
151 to treatment groups; sex cannot be determined at these stages. The AB (WT) genetic background was
152 used for generation of mutant and transgenic lines. Transgenic lines in this study include
153 Tg(*myl7:EGFP*) and Tg(*tbx5a:EGFP*;*tcf21:dsRED*). The *cygb2*^{801a} and the *gucy1a1* mutants were
154 generated using CRISPR-Cas9 genome editing as previously described[21] and guide RNAs are listed
155 in[21] and *Table S1*. Embryos were raised and screened for restriction enzyme site disruption (N1aIII)

156 using primers specific to exon 4 of *gucy1a1* (*Table S1*). The Tg(*myl7:EGFP*) and
157 Tg*(tbx5a:EGFP);*Tg*(tcf21:dsRED)* lines were crossed with *cygb2*^{801a} to produce
158 *cygb2*^{801a};Tg(myl7:EGFP), *cygb2*^{801a};Tg*(tbx5a:EGFP);*Tg*(tcf21:dsRED),* and wildtype sibling lines.
159

160 **2.2 Stroke Volume**

161 Stroke volumes were calculated from live imaging. To calculate end-diastolic volume (EDV) and end-
162 systolic volume (ESV) frames were identified from high-speed wide-field (bright-field and fluorescent)
163 time-lapse videos of beating zebrafish hearts at the moments of maximal and minimal ventricular cavity
164 size. The long-axis length (*L*) and short-axis diameter (*D*) of the ventricle were measured from frames
165 using the straight line tool in FIJI imaging software. EDV and ESV were calculated using the established
166 prolate spheroid model[30] according to the formula:

167 $V = \frac{\pi}{6} L D^2$

168 L represents ventricular long-axis length and D the diameter at mid-ventricle (*Figure S1*). Stroke volume
169 (SV) was derived as SV = EDV − ESV. Ventricle wall thickness was calculated at maximal and minimal
170 cavity size, identified from high-speed differential interference contrast (DIC) microscopy videos of
171 beating zebrafish hearts. The measurable area and length of the ventral-facing ventricle wall was
172 calculated using FIJI imaging software and the polygon selections and segmented line tool. Area was
173 divided by the length of the measured wall to generate a ratio-based metric of thickness. Bright field
174 and fluorescent images were captured using a Zeiss Axio Observer inverted microscope with attached
175 Axiocam 807 mono camera and a Leica M165FC with attached K3C camera.
176

177 **2.3 Ventricle Volume and morphology**

178 Whole mount confocal z-series and compiled z-projections were collected on paraformaldehyde fixed
179 zebrafish embryos from 16ss to 3 days post fertilization. Immuno-labeled embryos were mounted on
180 glass slides and imaged on a Nikon Ti2 inverted W1 spinning disk confocal microscope with attached

181 Hamamatsu sCMOS camera. Collected z-series were compiled into max projections and 3D objects
182 with surface renderings using FIJI and Imaris imaging software. Ventricle volume and wall thickness
183 were calculated using thresholding on selected regions of interest (ROI). Z-slices covering full depth
184 and width of ventricle were complied, images were converted to 8-bit and set to grey scale. To calculate
185 volume of myocardium, thresholding was set to black and white, area measurements for signal-positive
186 region were measured for each z-slice, summed, and multiplied by the distance between z-slices.
187 Ventricular lumen volume was calculated by measuring the area of signal-negative region within the
188 surrounding signal-positive region and summing the areas across z-slices and multiplying by the
189 distance between z-slices. To create a ratio-based metric to measure thickness across a 3-dimensional
190 structure, myocardium volume was divided by lumen volume. Cell density was calculated by dividing
191 total cardiomyocyte number by myocardium volume. Total ventricle cardiomyocyte number was
192 calculated using collected z-series and FIJI imaging software. Z-slices spanning the full depth and width
193 of the ventricle were compiled, and analyzed frame by frame, and EGFP-positive cardiomyocytes were
194 marked, tracked, and counted. Ventricle volume at 5 dpf was generated from z-series collected using
195 a Zeiss LS7 Lighsheet confocal microscope. Ventricle area of z-slices was calculated by thresholding
196 (Huang Over Under) of the EGFP positive region within a ROI defining the ventricle including the luminal
197 space. Using FIJI and open-source macro code ventricular volume was calculated by multiplying the
198 summed areas by the distance between z-slices. Progenitor cell fusion, cardiac disc, and heart tube
199 areas were calculated using thresholding of EGFP and CY5 positive areas in selected ROIs of max z-
200 projections collected using spinning disk confocal microscopy.
201

202 **2.4 In situ hybridization**

203 Whole-mount in situ hybridization was performed on paraformaldehyde fixed zebrafish embryos as
204 previously described[21] at 10-12ss and 28 hpf using riboprobes targeting *drl*, *kinase insert domain*
205 *receptor like* (*kdrl*), and *nkx2.5*. Transcripts were amplified by PCR and cDNA was obtained from pooled

206 embryos using transcript specific primers (*Table S1*). Images were collected using bright-field
207 microscopy on a Zeiss Discovery V.8 SteReo stereoscope with attached Axiocam 503 color camera,
208 brightness and contrast were unaltered, and images were formatted using FIJI imaging software. To
209 determine expression patterning variance, raw counts of phenotype rankings were used for statistical
210 comparisons with the Fishers exact test, percentages were plotted for graphical representation, ns -
211 not significant ≥ 0.05, * P≤ 0.05, ** P≤ 0.01, *** P≤ 0.001, **** P≤ 0.0001.
212

213 **Drug Exposure**

214 Carboxy-PTIO potassium salt (2-4-carboxyphenyl-4,4,5,5-tetramethylimidazoline-1-oxyl-3-oxide;
215 cPTIO, Sigma–C221) and BAY 582667 (Cinaciguat, Bay58, Sigma–SML1532) were diluted in DMSO
216 and used at final concentrations of 250μM and 120μM. (Z)-1-(N,N-diethylamino)diazen-1-ium-1,2-
217 diolate (DETA NONOate) (Cayman-82100) and (Z)-1-[N-(2-aminoethyl)-N-(2-
218 ammonioethyl)amino]diazen-1-ium-1,2-diolate (PAPA NONOate) (Cayman-2140) were resuspended
219 in sodium hydroxide and diluted in phosphate buffered saline at a final concentration of 500μM and
220 5.73μM. Drug route of exposure was administered through incubation in embryo media (E3).
221

222 **Immunohistochemistry**

223 Whole-mount immunohistochemistry was performed as previously described[21] using primary
224 antibodies for myosin heavy chain 6 (Developmental Studies Hybridoma Bank S46). Embryos were
225 mounted on glass slides with Vectashield Hardset Antifade Mounting Medium (H-1500-10) cover
226 slipped and imaged on a Nikon Ti2 inverted W1 spinning disk confocal microscope with attached
227 Hamamatsu sCMOS camera.
228
229
230

231 **cGMP ELISA**

232 cGMP levels in zebrafish embryos were measured by competitive ELISA following manufactures
233 protocol (Enzo-ADI-900-164). Embryos at 28 hpf were incubated in 250μM DETA NONOate for 30
234 minutes at 28.5 °C. Fifty embryos per sample were pooled and homogenized in 0.1M hydrochloric acid
235 on ice. Lysates were centrifuged and the supernatant was collected for analysis. Samples were
236 assayed in triplicate at two dilutions. cGMP concentration was calculated based on interpolation to the
237 standard curve using a 95% confidence interval.

238

239 **Cell culture**

240 The human type II alveolar epithelial cell line A549 was kindly provided by Dr. Alan Cross (Professor,
241 Department of Microbiology and Immunology, University of Maryland School of Medicine). A549 cells
242 were cultured in RPMI-1640 media (Gibco-11875093) containing Penicillin/Streptomycin (Sigma-
243 P4333) and fungizone (Amphoterecin B, Gibco-15290-026), and 10% fetal bovine serum (FBS) (Sigma-
244 F4135) at 37^0 Celsius and 5% carbon dioxide. Cell cultures were passaged a minimum of three times
245 before performing experiments.

246

247 **Small interfering RNA**

248 Dicer Substrate RNA duplexed small interfering RNAs targeting human cytoglobin were designed using
249 Integrated DNA Technologies "Predesigned DsiRNA Selection Tool". DsiRNA-mediated gene silencing
250 was performed by transfection of sub-confluent A549 monolayers using Lipofectamine RNAiMAX
251 transfection reagent (Thermo Fisher-13778030) and non-targeting DsiRNA and targeting si-CYGB 13.1
252 for 48 hours. To assess cell viability, transfected cells were pelleted and resuspended in a 1:1 mixture
253 of cell suspension and 0.4% Trypan Blue. Cells were counted using a hemocytometer in a 0.05μm
254 section. Cells excluding trypan blue were counted as live and cells stained with trypan blue were
255 counted as dead, viability was calculated as a percent of live cells to total cell number.

256 **Western Blot**

257 A549 cells were lysed on ice in RIPA buffer (Sigma-R0278) containing protease inhibitor (Halt 1X,
258 Thermo Fisher-1860932). Lysates were centrifuged at 12,500 RPM for 20 min at 4°C. The BCA assay
259 was used to determine total protein concentration. Samples were loaded for gel electrophoresis in 4-
260 20% precast gels (Bio-Rad-4561094) using 100 ug total protein per sample. Following electrophoresis
261 protein was transferred to polyvinylidene fluoride membranes. Membranes were blocked with 3%
262 bovine serum albumin (BSA) for 2 hours at room temperature under gentle agitation. Membranes were
263 probed with primary rabbit anti-CYGB (Sigma-HPA017757) diluted at 1:1000 in 1% BSA and 0.1%
264 Triton X100 in phosphate buffer saline (PBST) overnight at 4^0 Celsius. Following 3 consecutive 5-
265 minute washes at room temperature in PBST membranes were probed with anti-Rabbit IgG-HRP
266 (Abcam-131366) at 1:10,000 in PBST with 1% BSA for 1 hour at room temperature. Following 3
267 consecutive 5-minute washes at room temperature in a solution of PBST protein bands were visualized
268 using Clarity Max Western ECL substrate (Bio-Rad-1705060) following manufacturer's protocol and a
269 Bio-Rad ChemiDoc MP imaging box. Following 3 consecutive 5-minute washes with PBST at room
270 temperature membranes were stripped using Restore Western Blot Stripping Buffer (Thermo Scientific
271 21059). Blocking and probing procedure was repeated as before with primary anti-β-Actin antibody
272 (Sigma-A2066). Band intensity was normalized to β-Actin and quantified using FIJI imaging software.

273

274 **Wound healing assay**

275 A549 cells were seeded in 24-well plates at a density of 170,000 cells per well. After 24 hours cells
276 were transfected with 2.5pmol non-targeting DsiRNA, 1.25pmol and 2.5 pmol si-CYGB 13.1. 48 hours
277 post transfection a scratch was introduced with a 10µl pipette tip. Following the scratch cells were
278 washed with sterile 1x PBS and cultures were supplemented with RPMI-1640 media containing 10%
279 (FBS). Cultures were imaged at 0 and 24 hours post scratch on a Leica DM IL LED inverted microscope
280 using a 4X objective. Wound healing was assessed as precent migration into scratch area relative to

281 non-targeting DsiRNA. Image analysis was conducted using FIJI imaging software and the straight line
282 tool selected at lateral median.
283
284 **2.5 Statistical analysis**
285 Unless otherwise noted data are presented as mean ± SD, and statistical significance was determined
286 using an unpaired two-tailed *t*-test (or Mann–Whitney test for non-normal distributions), ns - not
287 significant ≥ 0.05, * P≤ 0.05, ** P≤ 0.01, *** P≤ 0.001, **** P≤ 0.0001.
288
289 **3. Results**
290 **Cytoglobin is required for ventricular development and cardiac function**
291 We previously defined a role for Cygb2 in cardiac laterality via regulation of cilia function. Here, we
292 investigated whether Cygb2 is required for cardiac morphogenesis and performance and whether these
293 are linked to laterality establishment. To visualize cardiac morphology we generated a *cygb2* mutant
294 line using the previously characterized *cygb2*^{801a} mutation[21] expressed in an established transgenic
295 reporter background expressing EGFP under the control of the *myosin light chain 7* (*myl7)* promoter.[23]
296 In zebrafish, *myl7* expression begins at approximately the 16ss stage in cardiomyocyte progenitors
297 regardless of eventual chamber contribution to the atrium or ventricle.[23] We analyzed *myl7:EGFP*
298 expression at 3 days post fertilization (dpf), when cardiac morphology is established, and the ventricle
299 and atrium exhibit coordinated contraction and robust cardiac function. We first quantified the area of
300 both cardiac chambers and observed a significant decrease in the ventricle of *cygb2*^{801a} embryos
301 compared to wildtype controls, (*Figure 1A–C, Movies S1-2*), while atrial area remained unchanged
302 (*Figure 1D*). To precisely assess performance, we measured EDV and ESV from in vivo high-speed
303 recordings and calculated SV using the prolate spheroid method *(Figure S1).* Ventricles of *cygb2*^{801a}
304 embryos showed a marked decrease in SV and EDV with no change in ESV (*Figure 1E–H*), consistent
305 with reduced diastolic filling rather than systolic impairment. As *cygb2*^{801a} embryos exhibited cardiac

306 laterality defects, we tested whether the ventricular defect might arise secondarily from laterality
307 disturbances. We compared SV between embryos with normal (situs solitus) and reversed (situs
308 inversus) cardiac orientation within each genotype and detected no differences, *cygb2*^{801a} embryos
309 displayed reduced SV relative to wildtype independent of cardiac left-right orientation (*Figure S2A–F*).
310 SV at 5dpf was assessed in the *myl7:EGFP* background and revealed that the phenotype persisted
311 (*Figure S3A–D, Movies S3-4*). Additionally, ventricle volume was assessed using light sheet confocal
312 microscopy on fixed *myl7:EGFP* samples and further supported the reduced ventricle phenotype and
313 persistence at 5 dpf in *cygb2*^{801a} compared to wildtype (*Figure S3E*). Collectively, these findings indicate
314 a stable structural hypoplasia rather than a transient developmental delay. Despite reduced chamber
315 size, ventricular cardiomyocyte number was unchanged (*Figure 1 I-J*). Instead, cells occupied a smaller
316 volume, yielding a more compact myocardium and a thicker ventricular wall (*Figure 1K–M*). These data
317 indicate that *cygb2* deficiency primarily affects ventricular morphogenesis and chamber remodeling,
318 not cardiomyocyte proliferation or survival. The reduced, thick-walled ventricle observed in *cygb2*^{801a}
319 embryos accompanied by reduced SV mirrors key structural features of HLHS and, given the
320 established role of Cygb2 in cilia-related laterality signaling, *cygb2* deficiency may represent a
321 mechanistically relevant model of HLHS-like ventricular hypoplasia.
322
323 **Nitric oxide restores ventricular size and function in *cygb2* mutants.**
324 We previously showed that Cygb2 regulates cardiac laterality determination[21] through NO signaling. To
325 test whether the reduced SV in *cygb2*^{801a} embryos depends on NO, we first confirmed the acute
326 physiological action of NO donors. Ten-minute exposure at 78 hpf to the pharmacological NO donor
327 DETA-NONOate (DETA) increased SV in both wildtype and *cygb2*^{801a} embryos *(Figure S4A-B),*
328 consistent with the reported hemodynamic effect of NO in teleost fish larvae[31] where the increase in
329 SV results from reduced afterload due to relaxation of the outflow vasculature. A fast-releasing NO
330 donor, PAPA-NONOate, produced a similar acute increase, validating the assay (*Figure S4C-D*). To

331 determine whether the altered ventricular structure and morphology could be rescued by NO
332 supplementation, we tested the effect of chronic DETA treatment. DETA was administered in a vehicle
333 (sodium hydroxide), which alone did not affect SV (*Figure S4E*). We performed chronic DETA
334 treatments from the 2ss stage to 3 dpf. Chronic exposure produced opposite outcomes depending on
335 genotype, in *cygb2*^{801a} embryos ventricular size increased with consequent rescue in SV, whereas in
336 wildtype embryos ventricular size was reduced, resulting in decreased SV (*Figure 2A-B*). Because
337 prolonged NO exposure affects cardiac morphogenesis rather than acute mechanics, these
338 bidirectional responses under identical dosing indicate that *cygb2* mutants possess a specific deficit in
339 NO-dependent developmental signaling, while excess NO in wildtype embryos disrupts the finely tuned
340 program governing ventricle morphogenesis. To provide further evidence supporting NO dependence,
341 we treated embryos at 2ss with the NO scavenger cPTIO to phenocopy the cardiac phenotype observed
342 in mutants (*Figure 2A,C*). As expected, ventricular volume was reduced by NO scavenging in wildtype
343 embryos and was further exacerbated in *cygb2*^{801a} embryos, consistent with a requirement for NO
344 signaling in normal ventricular development. A time course initiating DETA at stages from dome to 12ss
345 showed maximal rescue when treatment began at dome stage to 2ss, diminishing by 12ss (*Figure 2D*),
346 suggesting Cygb2-dependent NO signaling becomes critical for cardiac specification and
347 morphogenesis during early somitogenesis. Together, these findings demonstrate that *cygb2* is
348 required to maintain appropriate NO levels during early cardiac progenitor organization, thereby
349 ensuring proper ventricular morphogenesis and SV.
350
351 **Loss of Cygb2 disrupts early cardiomyocyte migration.**
352 Given that the ventricular phenotype observed in *cygb2*^{801a} embryos originates during early
353 development, we next examined cardiac morphogenesis to determine when these defects first emerge.
354 In zebrafish, cardiac progenitors originate bilaterally within the ALPM and progressively migrate toward
355 the midline, where they fuse to form the cardiac cone and subsequently the primitive heart tube. To

356 assess whether this process was altered in *cygb2* mutants, we analyzed the distribution of *myl7*-positive
357 cardiomyocyte precursors during heart field assembly. At 16ss when cardiomyocyte progenitors have
358 initiated migration but have not yet fused, *cygb2*^{801a} embryos displayed a significantly broader *myl7*-
359 positive domain compared with wildtype, indicating an expanded or delayed coalescence of cardiac
360 progenitors at this stage (*Figure 3A-C*). By 20ss, when the cardiac disc becomes morphologically visible
361 at the midline, the *myl7*-positive region remained wider and less compacted in *cygb2*^{801a} embryos,
362 occupying a larger total area relative to controls (*Figure 3D-F*). These results suggest that Cygb2 is
363 required for the coordinated medial convergence of cardiomyocyte progenitors during heart field
364 assembly. As development progressed, the cardiac tube of *cygb2*^{801a} embryos remained visibly smaller
365 than in wildtype. At 34 and 48 hpf, the ventricular area was significantly reduced indicating that the
366 morphogenetic defect persists through the stages of heart tube elongation and chamber ballooning,
367 whereas the atrium appeared morphologically normal throughout (*Figure S5A-H).* This suggests a
368 ventricle-specific effect consistent with the smaller, compact ventricular morphology observed at later
369 stages. To establish NO as a critical regulator throughout ventricular morphogenesis, embryos were
370 treated with the NO donor DETA beginning at 2ss. These treatments restored *myl7*-positive cardiac
371 field at 16 and 20ss (*Figure 3A-F)* and rescued ventricular area at 34 and 48 hpf (*Figure S5A-H*) to near
372 wildtype levels. These findings demonstrate that *cygb2* is essential for the proper migration and
373 coalescence of cardiac progenitors and for subsequent expansion of the ventricular chamber, and that
374 both processes depend on NO-mediated signaling.
375 Upon observing aberrant organization of cardiac progenitors during midline convergence and cardiac
376 disc formation in *cygb2*^{801a} embryos, we directly tested whether cell migratory behavior was disrupted
377 using an in vitro wound-healing assay in the human type II alveolar epithelial A549 cell line. *CYGB*
378 knockdown by small interfering RNA caused a dose-dependent reduction in cell migration into the
379 wound area (*Figure 3G-H*). CYGB expression knockdown efficiency and cell viability were confirmed
380 by Western Blot analysis (*Figure3I,J*) and viability assay (*Figure S6B*). These data suggest that

381 abnormal cardiac progenitor contribution to early heart structures may result from disruption of cellular
382 machinery regulating cell migration and/or cell adhesion and further indicate that Cygb-NO signaling
383 influences migratory behavior across cell types and species.
384
385 **Soluble guanylate cyclase is required for ventricle development and heart function.**
386 NO can signal through multiple mechanisms, including protein S-nitrosylation, nitration reactions and
387 formation of reactive nitrogen species. However, our data indicate that NO primarily signals through its
388 canonical receptor sGC. Upon ligand binding, NO-sGC catalyzes the conversion of guanosine
389 triphosphate (GTP) to cGMP, thereby initiating secondary downstream signaling events[32]. To test
390 whether the cardiac phenotype observed in *cygb2*^{801a} embryos depends on sGC, we generated an sGC
391 mutant (*gucy1a1*^{9bp}) using CRISPR/Cas9-mediated site-directed mutagenesis. Genomic DNA from
392 embryos derived from a maternal zygotic mutant line revealed a 9 bp deletion in exon 4 of the sGCα1
393 subunit, which was confirmed at the genomic and mRNA level by Sanger Sequencing (*Figure S7A*).
394 Loss of the normal transcript was validated by in situ hybridization using a 300 bp probe spanning the
395 edited region, which showed markedly reduced hybridization signal in *gucy1a1*^{9bp} embryos compared
396 to wildtype whereas a 1000 bp probe located downstream of the edited site produced comparable
397 staining in both mutants and wild type (*Figure S7B*). Functional loss of sGC activity in *gucy1a1*^{9bp}
398 embryos was confirmed by the absence of SV rescue following treatment with DETA and a
399 pharmacological sGC activator BAY 582667 (Bay58) (*Figure S7C-D*). Additionally, failure of DETA to
400 restore cGMP levels in *gucy1a1*^{9bp} compared to wildtype controls further validated the loss of function
401 (*Figure S7E*). In contrast, DETA treatment restored cGMP levels in *cygb2*^{801a} embryos,[21] supporting
402 the interpretation that Cygb2 functions upstream of sGC to regulate NO-dependent cGMP production
403 during cardiac development. To determine whether sGC disruption phenocopies the *cygb2*^{801a} cardiac
404 defect, we quantified ventricular performance in *gucy1a1*^{9bp} embryos using DIC microscopy and high-
405 speed imaging. SV was significantly reduced in *gucy1a1*^{9bp} compared with wildtype embryos, driven by

406 a decrease in EDV while ESV remained unchanged (*Figure 4A-E, Movies S5,6*). This pattern mirrors
407 the functional phenotype of *cygb2*^{801a} embryos, indicating that loss of sGCα1 function recapitulates the
408 diastolic filling defect observed in the *cygb2* mutant. Furthermore, replicating experiments done in
409 *cygb2* mutants we tested SV at 5dpf in *gucy1a1* mutants and found that in both reduced SV persisted
410 at later developmental stages (*Figure S3F, Movies S7,8*). To confirm that the observed phenotype
411 reflects disruption of a shared Cygb2-NO-sGC signaling pathway in both *cygb2*^{801a} *and gucy1a1*^{9bp}
412 mutants, we tested whether pharmacological activation of sGC in *cygb*^{801a} mutants could rescue cardiac
413 function. Treatment of *cygb*^{801a} mutants with the sGC activator Bay58 from 2ss to 34hpf fully restored
414 SV (*Figure 4F-H),* confirming a critical role for sGC signaling in ventricular formation. Notably, neither
415 DETA nor Bay58 rescued stroke volume in *gucy1a1*^{9bp} mutants, as expected (*Figure S7C-D*). To assess
416 a shared phenotype of increased ventricle wall thickness, measurements were performed on live
417 embryos at 3dpf. Wall thickness at diastole and systole was increased in *gucy1a1*^{9bp} (*Figure 4I-K,*
418 *Movies S5,6*), similar to that observed in *cygb2*^{801a} mutants (*Figure 4L-N, Movies S9,10*), indicating a
419 conserved phenotype across mutant models and analytic approaches. To determine whether NO-sGC
420 signaling contributes to this phenotype, *cygb2*^{801a} mutants were treated from 2ss to 34hpf with DETA
421 and Bay58. These conditions fully restored ventricular wall thickness (*Figure 4L-N),* supporting a role
422 for Cygb-NO-sGC in ventricular morphogenesis.
423

424 **NO-sGC signaling regulates early cardiac progenitor organization.**

425 To determine whether Cygb2 and Gucy1a1 act through a shared molecular pathway during early
426 cardiogenesis, we analyzed key markers of the ALPM at 10–12ss, when early cardiac and endothelial
427 progenitors are established. In wildtype embryos, *drl* expression appeared as bilateral short,
428 symmetrical stripes flanking the midline, marking anterior mesoderm that gives rise to cardiac and
429 vascular lineages. In both *cygb2*^{801a} and *gucy1a1*^{9bp} embryos, *drl* domains were elongated, thinner, and
430 extended posteriorly, indicating disrupted convergence and defective compaction of the ALPM (*Figure*

431 *5A*). Similarly, *kdrl*, which labels endothelial and endocardial progenitors, was expressed bilaterally in
432 compact domains close to the midline in wildtype embryos but it was elongated, more widely separated,
433 and extended posteriorly in *cygb2*^{801a} and *gucy1a1*^{9bp} mutants (*Figure S8*). This finding is consistent
434 with delayed or uncoordinated migration of endothelial/endocardial precursors. Despite these spatial
435 changes, signal intensity was not diminished, indicating that endothelial specification occurred
436 normally, but progenitor patterning shifted from anterior (endothelial/endocardial) toward more posterior
437 (hematopoietic) mesodermal domains. Expression of the early cardiac transcription factor nkx2.5 was
438 also altered at 10-12ss. In wildtype embryos, *nkx2.5* was expressed as two distinct, symmetrical
439 domains within the ALPM, whereas in *cygb2*^{801a} and *gucy1a1*^{9bp} mutants expression was frequently
440 asymmetric or spatially disorganized (*Figure 5B*), suggesting loss of coordination between left and right
441 cardiac fields. Importantly, wildtype siblings generated during establishment of the maternal-zygotic
442 *cygb2*^{801a} and *gucy1a1*^{9bp} lines were outcrossed to minimize potential CRISPR off-target effects and
443 displayed normal *drl*, *kdrl* and *nkx2.5* expression patterns at all developmental stages examined (*Figure*
444 *S9*). The *drl* expression patterning abnormalities were rescued in *cygb2*^{801a} embryos treated with either
445 DETA or Bay58 (Figure 5A), confirming that early ALPM organization and synchronized cardiac
446 specification depend on Cygb2-mediated NO–sGC signaling. Additionally, *nkx2.5* expression was also
447 partially normalized by DETA treatment, although the strongest normalization was achieved in embryos
448 treated with Bay58 (Figure 5B), confirming the importance of sGC signaling in this process. As *drl* marks
449 early cardiac precursors fields and *nkx2.5* labels a broader population encompassing later myocardial
450 progenitors, this differential rescue further supports the conclusion that NO–sGC signaling exerts its
451 strongest influence during the earliest stages of cardiac precursor organization and initial heart
452 structure formation.
453
454
455

456 **NO–sGC signaling rescues heart tube development.**

457 To assess whether early ALPM patterning defects persist during later stages of cardiogenesis, we
458 examined *drl*, and *nkx2.5* expression at 28 hpf, when the linear heart tube has formed and endothelial
459 and myocardial differentiation are underway. In wildtype embryos, *drl* expression is confined to the
460 developing vasculature and the endocardium; in contrast, *cygb2*^{801a} and *gucy1a1*^{9bp} embryos exhibited
461 reduced or absent *drl* expression in the heart tube (*Figure 6A*). This pattern is consistent with the shift
462 observed at earlier stages from anterior (endothelial/endocardial) toward more posterior
463 (hematopoietic) mesodermal domains. Consistently, *nkx2.5* expression in the ventricle was markedly
464 reduced in both *cygb2*^{801a} and *gucy1a1*^{9bp} embryos, indicating impaired myocardial contribution to this
465 region (*Figure 6B*). Treatment of *cygb2*^{801a} embryos with DETA or Bay58 restored *drl* and *nkx2.5*
466 expression patterns to near wildtype levels (*Figure 6A-B*). Together, these findings show that *cygb2*
467 and *gucy1a1* mutants share a common set of early and late ALPM abnormalities that can be corrected
468 by restoring NO-sGC signaling, linking early ALPM mis-patterning to the later emergence of a compact,
469 hypoplastic ventricle.

470

471 **4. Discussion**

472 Nitric oxide (NO) signaling is a central regulator of cardiovascular physiology, with established roles in
473 vascular tone, myocardial contractility, and hemodynamic homeostasis.[33-35] In contrast, the contribution
474 of NO signaling to early cardiac morphogenesis has been far less explored. Here, we show that Cygb2-
475 dependent NO–sGC signaling is required for ventricular formation during zebrafish heart development.
476 Loss of *cygb2* leads to a reduced SV associated with decreased ventricle volume, increased myocardial
477 wall thickness, elevated cellular density, and impaired diastolic filling. These defects arise from
478 abnormal migratory behavior of cardiac precursors, which display reduced migratory efficiency,
479 excessive cell-spreading, and subsequent hypercompaction within the forming heart tube. Importantly,
480 genetic loss of sGC (*gucy1a1*) fully phenocopies the *cygb2* mutant phenotype, and pharmacological

481 activation of NO-sGC signaling in *cygb2* mutants rescues ventricular volume, cardiac progenitor
482 migration, myocardial organization within the forming heart tube, and diastolic function. Together, these
483 data identify NO–sGC signaling downstream of Cygb2 as a central pathway coordinating myocardial
484 progenitor dynamics, ventricular morphogenesis, and functional maturation.

485 Cardiac progenitor migration is a fundamental driver of heart tube assembly and ventricular
486 morphogenesis and depends on tightly regulated cell polarity, adhesion turnover, and cytoskeletal
487 dynamics.[36-39] Disruption of these processes can profoundly alter chamber size and myocardial
488 architecture.[40,41] In this context, our data indicate that reduced NO–sGC signaling places cardiac
489 progenitors into a mechanically altered migratory state. NO-sGC-cGMP signaling is known to regulate
490 actomyosin contractility, focal adhesion turnover, and cortical tension across multiple cellular
491 contexts[42-44] and cytoglobin-dependent control of NO bioavailability represents a key upstream
492 determinant of this pathway[13,14]. Attenuation of NO–sGC signaling during development is therefore
493 predicted to stabilize cell–substrate and cell–cell adhesions, resulting in excessive cell spreading,
494 reduced migratory efficiency, and impaired tissue-level cellular rearrangements. When such
495 mechanically altered cells enter the confined environment of the forming heart tube, increased adhesion
496 and cortical tension can bias morphogenesis toward tissue compaction and elevated cellular packing
497 as demonstrated in epithelial and mesenchymal morphogenetic models.[45,46] These properties provide
498 a mechanistic basis for the increased ventricular cell density observed in *cygb2* mutants, together with
499 the resulting thick-walled ventricle and impaired diastolic function.

500 We previously demonstrated that Cygb2 localizes to motile cilia and regulates cilia-dependent left–right
501 patterning through NO–sGC signaling during early zebrafish development,[21] establishing that Cygb2-
502 dependent NO–sGC signaling operates during early developmental windows critical for laterality
503 specification. The present study extends this role to ventricular formation while showing that ventricular
504 defects do not arise directly from altered left–right axis specification (*Figure S2*). However, ventricular
505 morphogenesis may still depend on cilia-associated signaling while remaining independent of final

506 laterality outcomes. Here, we found that pharmacological restoration of NO–sGC signaling rescues
507 ventricular morphology only when administered during early windows encompassing laterality
508 determination and early somitogenesis, whereas later treatment fails to restore ventricular size and
509 stroke volume, indicating that ventricular morphogenesis is temporally linked to early cilia-associated
510 signaling events. During this developmental window, we found that *drl* and *kdrl* expression is spatially
511 displaced and expanded within the ALPM, phenotypes consistent with defective cardiac progenitor
512 migration rather than primary loss of cardiogenic identity[36,38,39,41]. Notably, *nkx2.5*, normally expressed
513 symmetrically by early somitogenesis[47] is found asymmetric in *cygb2* mutants, suggesting altered
514 organization of subsets of cardiac progenitors. Recent single-cell studies indicate that *nkx2.5* marks
515 transcriptionally distinct progenitor populations within the ALPM[29] supporting the idea that the disrupted
516 signaling perturbs progenitor composition rather than uniformly impairing cardiac fate. Early migratory
517 defects likely lead secondarily to impaired differentiation or maintenance programs later, as reflected
518 by the reduction of *nkx2.5* and *drl* expression within ventricular territories at 28 hpf.[48,49] Importantly,
519 dysregulation of NKX2-5 is associated with several forms of congenital heart disease in humans,
520 including ventricular septal defects, tetralogy of Fallot, and HLHS, underscoring the relevance of these
521 findings to human cardiac pathogenesis.[47,50,51]

522 Sequencing studies have identified enrichment of rare variants in cilia and ciliopathy-associated genes
523 in subsets of HLHS patient cohorts,[4] supporting a framework in which cilia-dependent pathways
524 contribute to disease susceptibility in a subset of patients. Within this framework, zebrafish models
525 exhibiting reduced ventricular size with compact myocardium have emerged as informative systems for
526 studying cardiac morphogenesis and HLHS-like phenotypes.[9,49] In our *cygb2* mutant model, HLHS-like
527 ventricular hypoplasia originates from early events concomitant with cilia-dependent processes
528 involved in left-right patterning. Our data indicate two possible mechanistic pathways underlying this
529 phenotype. In one scenario, impaired NO-sGC signaling caused by loss of Cygb2 directly disrupts the
530 coordination of cardiac progenitor migration, regional specification, and ventricle expansion, leading to

531 reduced ventricular growth. In a second, distinct scenario, loss of Cygb2 perturbs cilia-dependent
532 processes that regulate early cardiac morphogenesis and myocardial growth, beyond their established
533 role in cardiac laterality, through downstream effects on progenitor deployment and tissue remodeling,[50]
534 independent of left–right axis determination. These mechanisms are not mutually exclusive and may
535 interact in the multigenic context of human HLHS, where combined defects in NO signaling and cilia-
536 associated pathways could converge on shared morphogenetic processes controlling ventricular
537 development. The *cygb2 and gucy1a1* models characterized here converge on the hallmark ventricular
538 phenotype of HLHS while revealing a distinct initiating axis centered on Cygb-dependent NO–sGC
539 signaling. Together with prior work demonstrating that modulation of NO bioavailability influences
540 myocardial plasticity and regeneration,[52] these findings establish NO–sGC signaling as a tractable
541 developmental pathway whose disruption leads to ventricular hypoplasia and whose restoration is
542 sufficient to rescue ventricular structure and function. Our data indicate that pharmacological activation
543 of sGC, previously unexplored in the context of hypoplastic ventricular disease, can restore ventricular
544 structure and function in HLHS-like phenotypes in vivo. These results position zebrafish as a valuable
545 model for interrogating early developmental mechanisms underlying ventricular hypoplasia and for
546 assessing sGC-targeted interventions in CHD.
547
548
549
550
551
552
553
554
555

556 **Author Contributions**

557 Adam Clark, Paola Corti designed and conducted experiments, analyzed data, and wrote the
558 manuscript; Muddassar Iqbal and Rasmus Hejlesen reviewed the manuscript; Rasmus Hejlesen
559 constructed a data set for transcript variance analysis; Weng Tzu-Ting conducted in situ hybridization
560 experiments; Muddassar Iqbal designed, conducted; and analyzed data for wound healing assay
561 experiments; Akueba Bruce conducted zebrafish husbandry and genotyping.

562

563 **Acknowledgements**

564 We are thankful to the University of Maryland School of Medicine Center for Innovative Biomedical
565 Resources; Confocal Microscopy Core (Dr. Joseph Mauban and Dr. Shilpa Kumar) and Translational
566 Genomics Lab, for invaluable assistance in Imaging and Sanger Sequencing.

567

568 **Conflict of Interest:** The authors declare no competing interests that influence the work reported in
569 this paper.

570

571 **Funding**

572 This work was supported by National Institutes of Health under awards number 5T32AR7592-27 and
573 NHL168775.

574

575 **Data availability**

576 The data used to produce this article will be shared at reasonable request to the corresponding author.

577

578

579

580

581 **References**

582 1. Iascone M, Ciccone R, Galletti L, Marchetti D, Seddio F, Lincesso AR, Pezzoli L, Vetro A,
583 Barachetti D, Boni L, Federici D, Soto AM, Comas JV, Ferrazzi P, Zuffardi O. Identification of
584 de novo mutations and rare variants in hypoplastic left heart syndrome. *Clin Genet*
585 2012;**81**:542–554.

586 2. Yagi H, Liu X, Gabriel GC, Wu Y, Peterson K, Murray SA, Aronow BJ, Martin LJ, Benson DW, Lo
587 CW. The Genetic Landscape of Hypoplastic Left Heart Syndrome. *Pediatr Cardiol*
588 2018;**39**:1069–1081.

589 3. Grossfeld P, Nie S, Lin L, Wang L, Anderson RH. Hypoplastic Left Heart Syndrome: A New
590 Paradigm for an Old Disease? *J Cardiovasc Dev Dis* 2019;**6**.

591 4. Gabriel GC, Lo CW. Left-right patterning in congenital heart disease beyond heterotaxy. *Am J Med*
592 *Genet C Semin Med Genet* 2020;**184**:90–96.

593 5. Lin AE, Krikov S, Riehle-Colarusso T, Frias JL, Belmont J, Anderka M, Geva T, Getz KD, Botto LD,
594 National Birth Defects Prevention S. Laterality defects in the national birth defects prevention
595 study (1998-2007): birth prevalence and descriptive epidemiology. *Am J Med Genet A*
596 2014;**164A**:2581–2591.

597 6. Becker DJ, Islam S, Geiger JD. Biliary atresia associated with hypoplastic left heart syndrome: a
598 case report and review of the literature. *J Pediatr Surg* 2004;**39**:1411–1413.

599 7. Stankiewicz P, Sen P, Bhatt SS, Storer M, Xia Z, Bejjani BA, Ou Z, Wiszniewska J, Driscoll DJ,
600 Maisenbacher MK, Bolivar J, Bauer M, Zackai EH, McDonald-McGinn D, Nowaczyk MM,
601 Murray M, Hustead V, Mascotti K, Schultz R, Hallam L, McRae D, Nicholson AG, Newbury R,
602 Durham-O'Donnell J, Knight G, Kini U, Shaikh TH, Martin V, Tyreman M, Simonic I, Willatt L,
603 Paterson J, Mehta S, Rajan D, Fitzgerald T, Gribble S, Prigmore E, Patel A, Shaffer LG, Carter
604 NP, Cheung SW, Langston C, Shaw-Smith C. Genomic and genic deletions of the FOX gene

605 cluster on 16q24.1 and inactivating mutations of FOXF1 cause alveolar capillary dysplasia and
606 other malformations. *Am J Hum Genet* 2009;**84**:780–791.
607 8. Huseynova RA, Bin Mahmoud LA, Abdelrahim A, Alroiedy MA, Huseynov O. Polysplenia syndrome
608 with complex heart disease and jejunal atresia with malrotation in neonate: A case report. *Clin*
609 *Case Rep* 2020;**8**:848–851.
610 9. Huang M, Akerberg AA, Zhang X, Yoon H, Joshi S, Hallinan C, Nguyen C, Pu WT, Haigis MC,
611 Burns CG, Burns CE. Intrinsic myocardial defects underlie an Rbfox-deficient zebrafish model
612 of hypoplastic left heart syndrome. *Nat Commun* 2022;**13**:5877.
613 10. Yagi H, Lo CW. Left-Sided Heart Defects and Laterality Disturbance in Hypoplastic Left Heart
614 Syndrome. *J Cardiovasc Dev Dis* 2023;**10**.
615 11. Liu X, Yagi H, Saeed S, Bais AS, Gabriel GC, Chen Z, Peterson KA, Li Y, Schwartz MC,
616 Reynolds WT, Saydmohammed M, Gibbs B, Wu Y, Devine W, Chatterjee B, Klena NT, Kostka
617 D, de Mesy Bentley KL, Ganapathiraju MK, Dexheimer P, Leatherbury L, Khalifa O, Bhagat A,
618 Zahid M, Pu W, Watkins S, Grossfeld P, Murray SA, Porter GA, Jr., Tsang M, Martin LJ,
619 Benson DW, Aronow BJ, Lo CW. The complex genetics of hypoplastic left heart syndrome. *Nat*
620 *Genet* 2017;**49**:1152–1159.
621 12. Trent JT, 3rd, Hargrove MS. A ubiquitously expressed human hexacoordinate hemoglobin. *J Biol*
622 *Chem* 2002;**277**:19538–19545.
623 13. Corti P, Ieraci M, Tejero J. Characterization of zebrafish neuroglobin and cytoglobins 1 and 2:
624 Zebrafish cytoglobins provide insights into the transition from six-coordinate to five-coordinate
625 globins. *Nitric Oxide* 2016;**53**:22–34.
626 14. Amdahl MB, Sparacino-Watkins CE, Corti P, Gladwin MT, Tejero J. Efficient Reduction of
627 Vertebrate Cytoglobins by the Cytochrome b(5)/Cytochrome b(5) Reductase/NADH System.
628 *Biochemistry* 2017;**56**:3993–4004.

629 15. Reeder BJ, Ukeri J. Strong modulation of nitrite reductase activity of cytoglobin by disulfide bond
630 oxidation: Implications for nitric oxide homeostasis. *Nitric Oxide* 2018;**72**:16–23.
631 16. Halligan KE, Jourd'heuil FL, Jourd'heuil D. Cytoglobin is expressed in the vasculature and
632 regulates cell respiration and proliferation via nitric oxide dioxygenation. *J Biol Chem*
633 2009;**284**:8539–8547.
634 17. Gardner AM, Cook MR, Gardner PR. Nitric-oxide dioxygenase function of human cytoglobin with
635 cellular reductants and in rat hepatocytes. *J Biol Chem* 2010;**285**:23850–23857.
636 18. Tejero J, Shiva S, Gladwin MT. Sources of Vascular Nitric Oxide and Reactive Oxygen Species
637 and Their Regulation. *Physiol Rev* 2019;**99**:311–379.
638 19. Zweier JL, Ilangovan G. Regulation of Nitric Oxide Metabolism and Vascular Tone by Cytoglobin.
639 *Antioxid Redox Signal* 2020;**32**:1172–1187.
640 20. Zweier JL, Hemann C, Kundu T, Ewees MG, Khaleel SA, Samouilov A, Ilangovan G, El-Mahdy
641 MA. Cytoglobin has potent superoxide dismutase function. *Proc Natl Acad Sci U S A*
642 2021;**118**.
643 21. Rochon ER, Xue J, Mohammed MS, Smith C, Hay-Schmidt A, DeMartino AW, Clark A, Xu Q, Lo
644 CW, Tsang M, Tejero J, Gladwin MT, Corti P. Cytoglobin regulates NO-dependent cilia motility
645 and organ laterality during development. *Nat Commun* 2023;**14**:8333.
646 22. Yelon D. Cardiac patterning and morphogenesis in zebrafish. *Dev Dyn* 2001;**222**:552–563.
647 23. Kemmler CL, Riemslagh FW, Moran HR, Mosimann C. From Stripes to a Beating Heart: Early
648 Cardiac Development in Zebrafish. *J Cardiovasc Dev Dis* 2021;**8**.
649 24. Felker A, Prummel KD, Merks AM, Mickoleit M, Brombacher EC, Huisken J, Panakova D,
650 Mosimann C. Continuous addition of progenitors forms the cardiac ventricle in zebrafish. *Nat*
651 *Commun* 2018;**9**:2001.

652 25. Paffett-Lugassy N, Novikov N, Jeffrey S, Abrial M, Guner-Ataman B, Sakthivel S, Burns CE,
653 Burns CG. Unique developmental trajectories and genetic regulation of ventricular and outflow
654 tract progenitors in the zebrafish second heart field. *Development* 2017;**144**:4616–4624.
655 26. Hirokawa N, Tanaka Y, Okada Y. Left-right determination: involvement of molecular motor KIF3,
656 cilia, and nodal flow. *Cold Spring Harb Perspect Biol* 2009;**1**:a000802.
657 27. Mosimann C, Panakova D, Werdich AA, Musso G, Burger A, Lawson KL, Carr LA, Nevis KR,
658 Sabeh MK, Zhou Y, Davidson AJ, DiBiase A, Burns CE, Burns CG, MacRae CA, Zon LI.
659 Chamber identity programs drive early functional partitioning of the heart. *Nat Commun*
660 2015;**6**:8146.
661 28. Pashmforoush M, Lu JT, Chen H, Amand TS, Kondo R, Pradervand S, Evans SM, Clark B,
662 Feramisco JR, Giles W, Ho SY, Benson DW, Silberbach M, Shou W, Chien KR. Nkx2-5
663 pathways and congenital heart disease; loss of ventricular myocyte lineage specification leads
664 to progressive cardiomyopathy and complete heart block. *Cell* 2004;**117**:373–386.
665 29. Coskun H, Wang Y, Gao X, Chen K, Geoffrey Burns C, Burns CE. 3D spatial organization of
666 heterogeneous nkx2.5+ progenitors in the zebrafish heart field pre-patterns cardiovascular
667 development. *Nat Commun* 2025;**16**:11624.
668 30. Yalcin HC, Amindari A, Butcher JT, Althani A, Yacoub M. Heart function and hemodynamic
669 analysis for zebrafish embryos. *Dev Dyn* 2017;**246**:868–880.
670 31. Fritsche R, Schwerte T, Pelster B. Nitric oxide and vascular reactivity in developing zebrafish,
671 Danio rerio. *Am J Physiol Regul Integr Comp Physiol* 2000;**279**:R2200–2207.
672 32. Arnold WP, Mittal CK, Katsuki S, Murad F. Nitric oxide activates guanylate cyclase and increases
673 guanosine 3':5'-cyclic monophosphate levels in various tissue preparations. *Proc Natl Acad Sci*
674 *U S A* 1977;**74**:3203–3207.
675 33. Ignarro LJ. Nitric Oxide: A Unique Endogenous Signaling Molecule in Vascular Biology (Nobel
676 Lecture). *Angew Chem Int Ed Engl* 1999;**38**:1882–1892.

677 34. Gladwin MT. Deconstructing endothelial dysfunction: soluble guanylyl cyclase oxidation and the
678 NO resistance syndrome. *J Clin Invest* 2006;**116**:2330–2332.
679 35. Forstermann U, Sessa WC. Nitric oxide synthases: regulation and function. *Eur Heart J*
680 2012;**33**:829–837, 837a–837d.
681 36. Stainier DY. Zebrafish genetics and vertebrate heart formation. *Nat Rev Genet* 2001;**2**:39–48.
682 37. Buckingham SD, Ali DW. Computer simulations of high-pass filtering in zebrafish larval muscle
683 fibres. *J Exp Biol* 2005;**208**:3055–3063.
684 38. Abu-Issa R, Kirby ML. Heart field: from mesoderm to heart tube. *Annu Rev Cell Dev Biol*
685 2007;**23**:45–68.
686 39. Bakkers J. Zebrafish as a model to study cardiac development and human cardiac disease.
687 *Cardiovasc Res* 2011;**91**:279–288.
688 40. Hutson MR, Kirby ML. Model systems for the study of heart development and disease. Cardiac
689 neural crest and conotruncal malformations. *Semin Cell Dev Biol* 2007;**18**:101–110.
690 41. Vincent SD, Buckingham ME. How to make a heart: the origin and regulation of cardiac progenitor
691 cells. *Curr Top Dev Biol* 2010;**90**:1–41.
692 42. Surks HK, Mochizuki N, Kasai Y, Georgescu SP, Tang KM, Ito M, Lincoln TM, Mendelsohn ME.
693 Regulation of myosin phosphatase by a specific interaction with cGMP- dependent protein
694 kinase Ialpha. *Science* 1999;**286**:1583–1587.
695 43. Schlossmann J, Hofmann F. cGMP-dependent protein kinases in drug discovery. *Drug Discov*
696 *Today* 2005;**10**:627–634.
697 44. Prysyazhna O, Rudyk O, Eaton P. Single atom substitution in mouse protein kinase G eliminates
698 oxidant sensing to cause hypertension. *Nat Med* 2012;**18**:286–290.
699 45. Lecuit T, Lenne PF. Cell surface mechanics and the control of cell shape, tissue patterns and
700 morphogenesis. *Nat Rev Mol Cell Biol* 2007;**8**:633–644.

701 46. Heisenberg CP, Bellaiche Y. Forces in tissue morphogenesis and patterning. *Cell* 2013;**153**:948–
702 962.
703 47. Sultana N, Nag K, Hoshijima K, Laird DW, Kawakami A, Hirose S. Zebrafish early cardiac
704 connexin, Cx36.7/Ecx, regulates myofibril orientation and heart morphogenesis by establishing
705 Nkx2.5 expression. *Proc Natl Acad Sci U S A* 2008;**105**:4763–4768.
706 48. Moorman AF, Christoffels VM. Cardiac chamber formation: development, genes, and evolution.
707 *Physiol Rev* 2003;**83**:1223–1267.
708 49. Liu J, Stainier DY. Zebrafish in the study of early cardiac development. *Circ Res* 2012;**110**:870–
709 874.
710 50. Sutherland MJ, Ware SM. Disorders of left-right asymmetry: heterotaxy and situs inversus. *Am J*
711 *Med Genet C Semin Med Genet* 2009;**151C**:307–317.
712 51. George V, Colombo S, Targoff KL. An early requirement for nkx2.5 ensures the first and second
713 heart field ventricular identity and cardiac function into adulthood. *Dev Biol* 2015;**400**:10–22.
714 52. Rochon ER, Missinato MA, Xue J, Tejero J, Tsang M, Gladwin MT, Corti P. Nitrite Improves Heart
715 Regeneration in Zebrafish. *Antioxid Redox Signal* 2020;**32**:363–377.
716
717
718
719
720
721
722
723
724
725

Figures

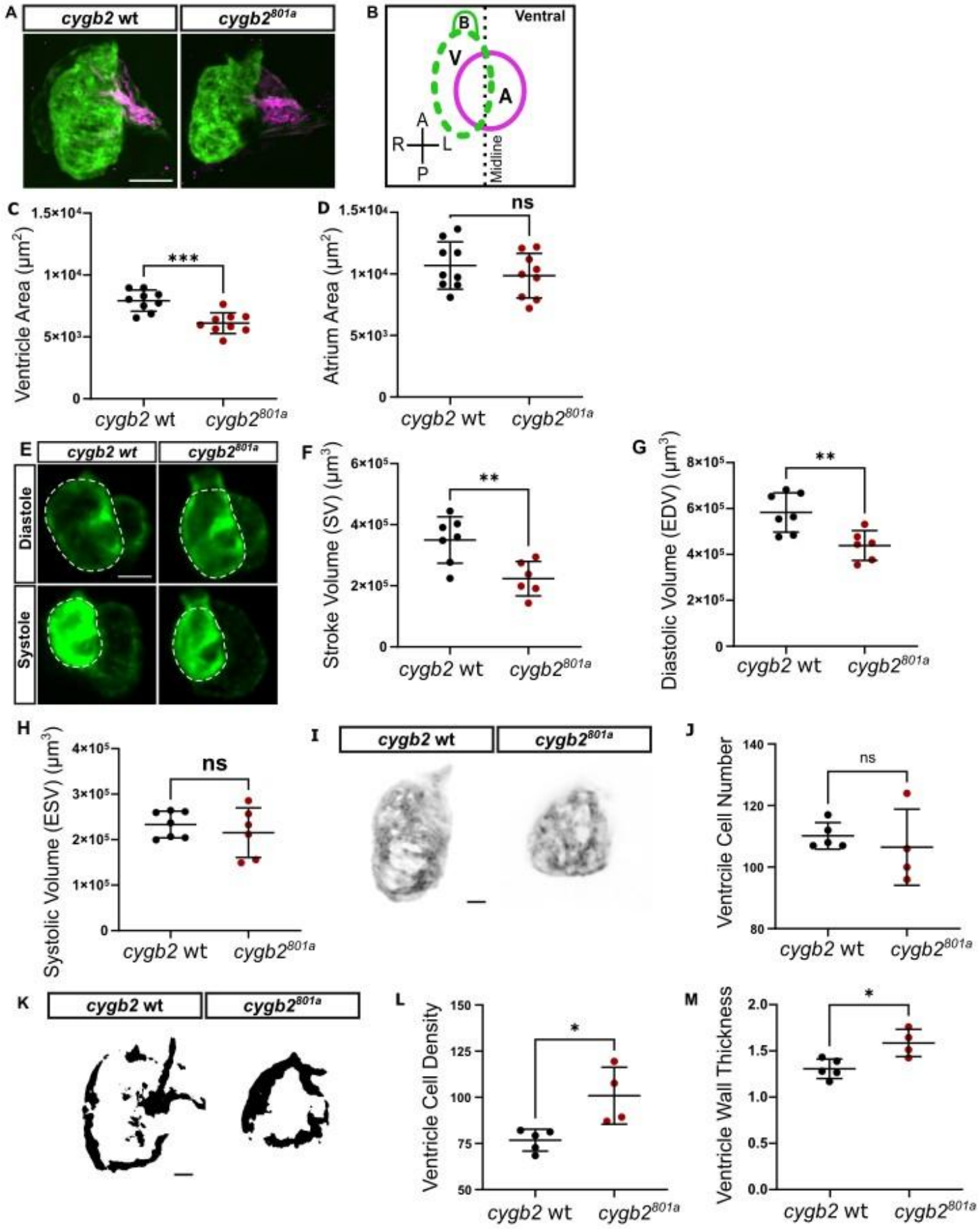
A
cygb2 wt
cygb2801a
B
Ventral
B
V
A
A
R
L
P
Midline
C
Ventricle Area (μm2)
1.5×104
1×104
5×103
0
***
cygb2 wt
cygb2801a
D
Atrium Area (μm2)
1.5×104
1×104
5×103
0
ns
cygb2 wt
cygb2801a
E
cygb2 wt
cygb2801a
Diastole
Systole
F
Stroke Volume (SV) (μm3)
6×105
4×105
2×105
0
**
cygb2 wt
cygb2801a
G
Diastolic Volume (EDV) (μm3)
8×105
6×105
4×105
2×105
0
**
cygb2 wt
cygb2801a
H
Systolic Volume (ESV) (μm3)
4×105
3×105
2×105
1×105
0
ns
cygb2 wt
cygb2801a
I
cygb2 wt
cygb2801a
J
Ventrcile Cell Number
140
120
100
80
ns
cygb2 wt
cygb2801a
K
cygb2 wt
cygb2801a
L
Ventricle Cell Density
150
125
100
75
50
*
cygb2 wt
cygb2801a
M
Ventricle Wall Thickness
2.0
1.5
1.0
0.5
0.0
*
cygb2 wt
cygb2801a

Figure 1

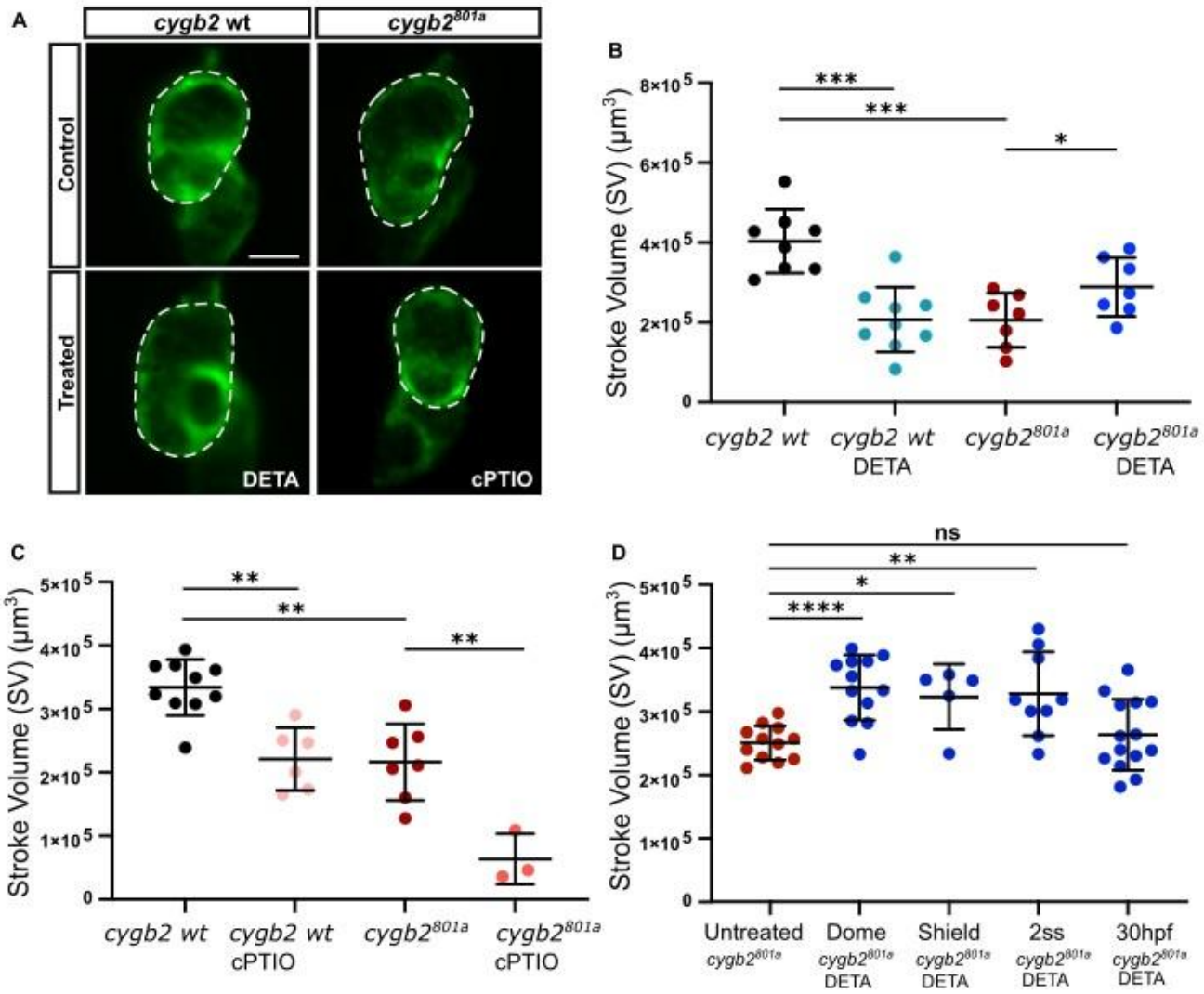
A
cygb2 wt
cygb2801a
Control
Treated
DETA
cPTIO
B
Stroke Volume (SV) (µm3)
8×105
6×105
4×105
2×105
0
***
***
*
cygb2 wt
cygb2 wt DETA
cygb2801a
cygb2801a DETA
C
Stroke Volume (SV) (µm3)
5×105
4×105
3×105
2×105
1×105
0
**
**
**
cygb2 wt
cygb2 wt cPTIO
cygb2801a
cygb2801a cPTIO
D
Stroke Volume (SV) (µm3)
5×105
4×105
3×105
2×105
1×105
0
ns
**
*
****
Untreated cygb2801a
Dome cygb2801a DETA
Shield cygb2801a DETA
2ss cygb2801a DETA
30hpf cygb2801a DETA

Figure 2

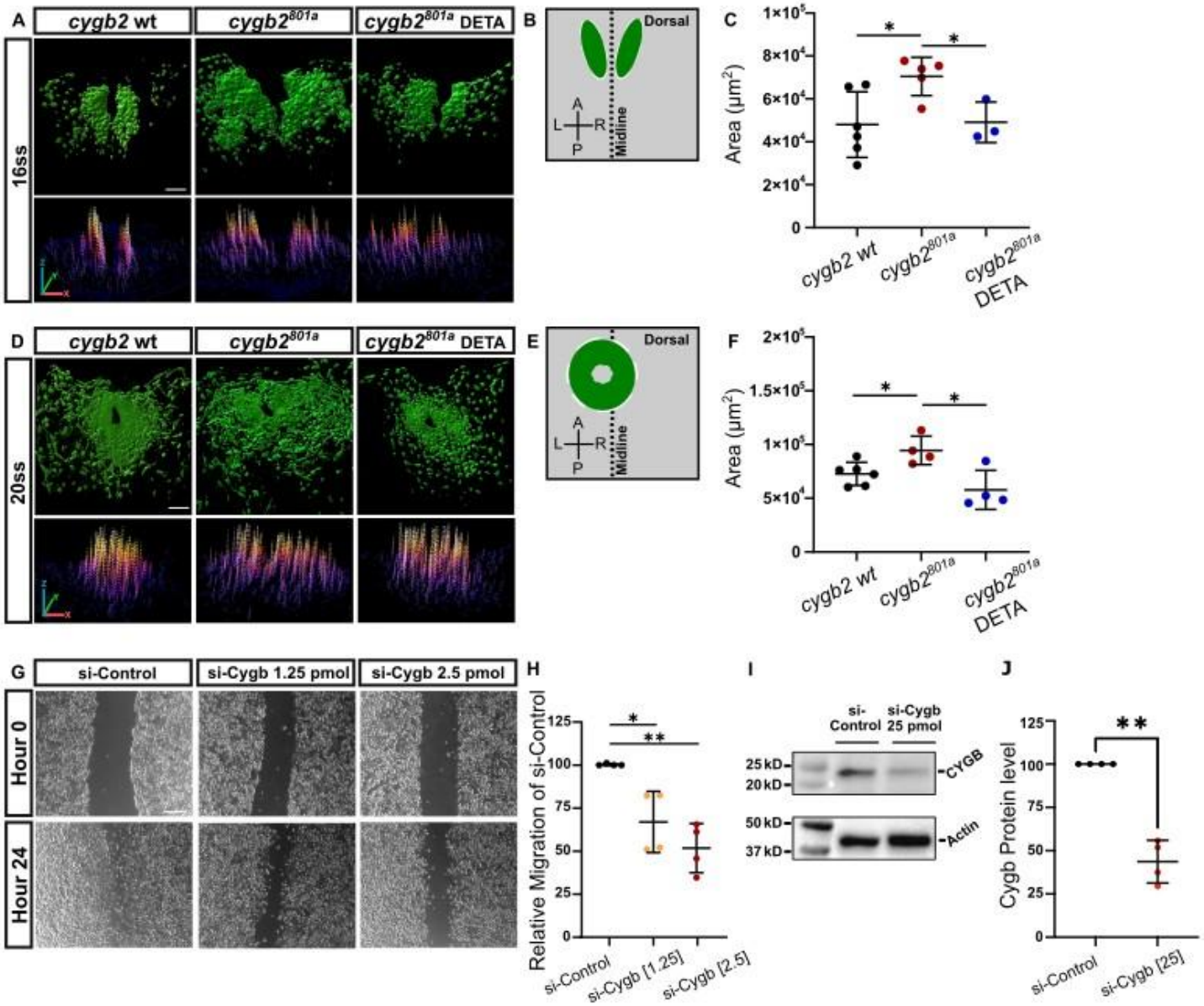
A
cygb2 wt
cygb2801a
cygb2801a DETA
16ss
B
Dorsal
A
L
R
P
Midline
C
Area (μm2)
1×105
8×104
6×104
4×104
2×104
0
*
*
cygb2 wt
cygb2801a
cygb2801a DETA
D
cygb2 wt
cygb2801a
cygb2801a DETA
20ss
E
Dorsal
A
L
R
P
Midline
F
Area (μm2)
2×105
1.5×105
1×105
5×104
0
*
*
cygb2 wt
cygb2801a
cygb2801a DETA
G
si-Control
si-Cygb 1.25 pmol
si-Cygb 2.5 pmol
Hour 0
Hour 24
H
Relative Migration of si-Control
125
100
75
50
25
0
*
**
si-Control
si-Cygb [1.25]
si-Cygb [2.5]
I
si-Control
si-Cygb 25 pmol
25 kD
20 kD
CYGB
50 kD
37 kD
Actin
J
Cygb Protein level
125
100
75
50
25
0
**
si-Control
si-Cygb [25]

Figure 3

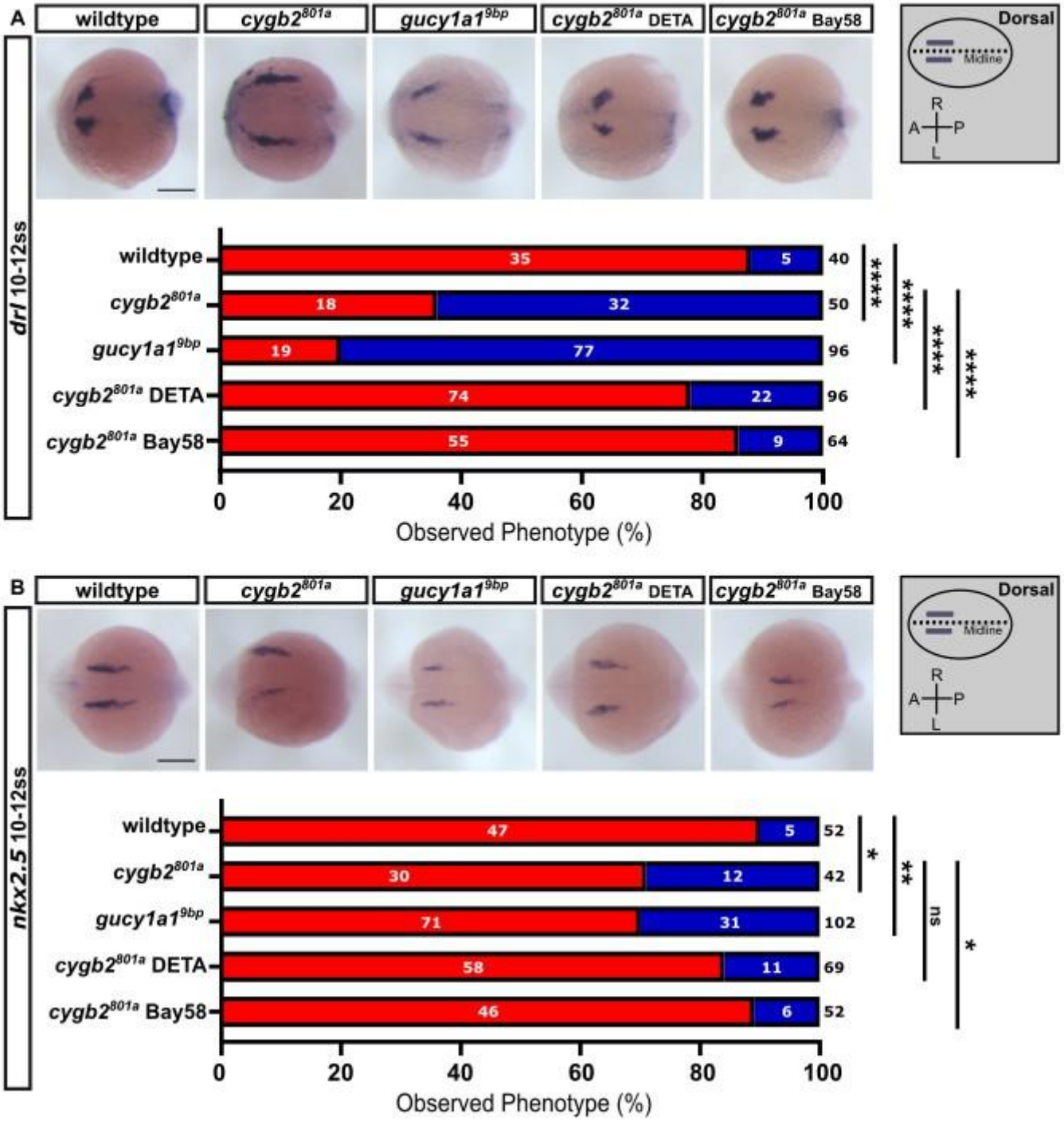
A
wildtype
cygb2801a
gucy1a19bp
cygb2801a DETA
cygb2801a Bay58
Dorsal
Midline
R
A
P
L
drl 10-12ss
wildtype
cygb2801a
gucy1a19bp
cygb2801a DETA
cygb2801a Bay58
35
5
40
18
32
50
19
77
96
74
22
96
55
9
64
****
****
****
****
0
20
40
60
80
100
Observed Phenotype (%)
B
wildtype
cygb2801a
gucy1a19bp
cygb2801a DETA
cygb2801a Bay58
Dorsal
Midline
R
A
P
L
nkx2.5 10-12ss
wildtype
cygb2801a
gucy1a19bp
cygb2801a DETA
cygb2801a Bay58
47
5
52
30
12
42
71
31
102
58
11
69
46
6
52
*
**
ns
*
0
20
40
60
80
100
Observed Phenotype (%)

1**Figure 5**

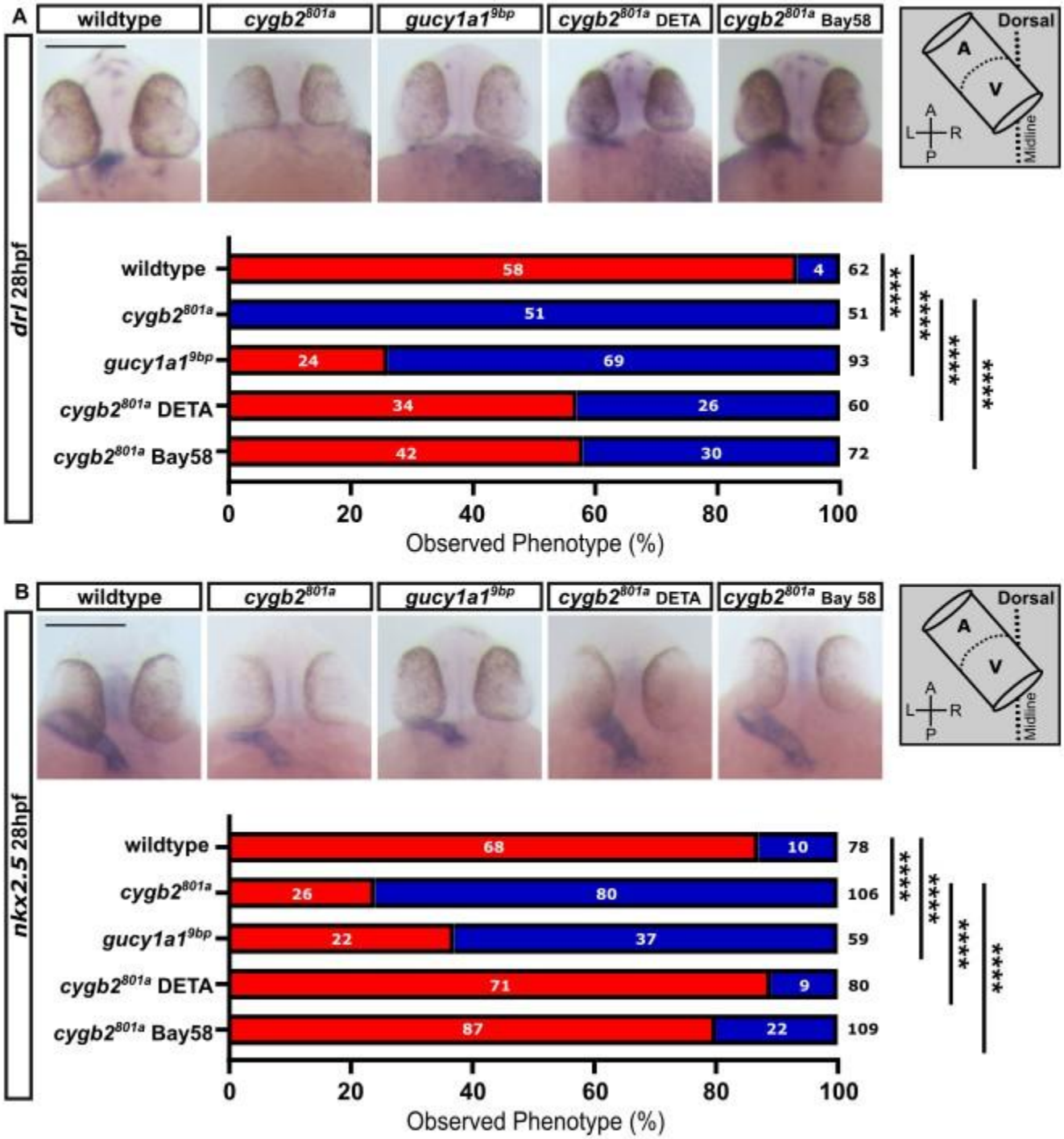
A
wildtype
cygb2801a
gucy1a19bp
cygb2801a DETA
cygb2801a Bay58
Dorsal
A
V
L
R
P
Midline
drl 28hpf
wildtype
cygb2801a
gucy1a19bp
cygb2801a DETA
cygb2801a Bay58
58
4
62
51
51
24
69
93
34
26
60
42
30
72
****
****
****
****
0
20
40
60
80
100
Observed Phenotype (%)
B
wildtype
cygb2801a
gucy1a19bp
cygb2801a DETA
cygb2801a Bay 58
Dorsal
A
V
L
R
P
Midline
nkx2.5 28hpf
wildtype
cygb2801a
gucy1a19bp
cygb2801a DETA
cygb2801a Bay58
68
10
78
26
80
106
22
37
59
71
9
80
87
22
109
****
****
****
****
0
20
40
60
80
100
Observed Phenotype (%)

Figure 6

783 **Figure Legends**

784

785 **Figure 1. Loss of *cygb2* leads to ventricular hypoplasia and reduced cardiac output. (A)**
786 Representative confocal projections of *cygb2wt*;Tg*(myl7*:EGFP) and *cygb2*^{801a}*;*Tg*(myl7*:EGFP) hearts
787 at 3 dpf, immuno-labeled for MYH6 (EGFP, green; MYH6, magenta). Scale bar, 50µm **(B)** Schematic
788 illustrating heart chamber anatomy and cardiac orientation. A-atrium; V-ventricle; B-bulbus arteriosus
789 **(C-D)** Comparison of ventricle and atrium area. **(E)** Representative frames from fluorescence time-
790 lapse imaging of live *cygb2wt*;Tg*(myl7*:EGFP) and *cygb2*^{801a}*;*Tg*(myl7*:EGFP) embryos 3 dpf showing
791 ventricle volume at diastole and systole, dashed white line demarcates the ventricle (EGFP, green).
792 Scale bar, 50 µm. **(F-H)** Comparison of stroke volume, diastolic volume and systolic volume. **(I)**
793 Representative confocal projections of ventricles at 3 dpf, images are greyscale converted and inverted
794 to highlight cardiomyocyte density. Scale bar, 20µm. **(J)** Comparison of ventricle cell number. **(K)**
795 Representative confocal z-slices at ventricular midpoint. Images were converted to greyscale signal
796 positive area (ventricular myocardium) shown in black. **(L)** Comparison of cardiomyocyte density. **(M)**
797 Comparison of ventricular wall thickness. Student t-Test; *ns*, not significant; *p<0.05;
798 **p<0.01;***p<0.001

799

800 **Figure 2. NO rescues the *cygb2* mutant phenotype whereas NO scavenging phenocopies the**
801 **mutant. (A)** Representative frames from fluorescent time-lapse imaging of live
802 *cygb2wt*;Tg(*myl7*:EGFP) and *cygb2*^{801a};Tg(*myl7*:EGFP) mutants at 3dpf, showing the effect of
803 treatment with a pharmacological NO scavenger (cPTIO) and NO donor (DETA) on diastolic volume
804 (EGFP, green). Scale bar, 50µm. **(B)** Comparison of SV at 3dpf in untreated control and DETA treated,
805 and **(C)** cPTIO treated embryos, treatments starting at 2ss. **(D)** Comparison of stroke volumes following
806 chronic treatments starting at different developmental stages (dome, shield, 2ss, and 30hpf). Student
807 t-Test; *ns*, not significant; *p<0.05; **p<0.01;***p<0.001; ****p<0.0001.

808

809 **Fig. 3. *cygb2* mutants show defective cardiac progenitors migration, and CYGB knockdown**
810 **inhibits cell migration in human airway epithelial cell culture. (A, D)** 3D surface rendering and
811 surface plots from *cygb2wt*;Tg(*myl7*:EGFP) and *cygb2*^{801a};Tg(*myl7*:EGFP) showing cardiac progenitors
812 at midline convergence (16 ss) and cardiac disc (20 ss), renderings and surface plots generated from
813 whole-mount confocal z-series (EGFP, green). DETA treatment starting at 2ss. Scale bar, 50μm. (**B, E**)
814 Schematics illustrating cardiac progenitor organization and embryonic orientation. **(C, F)** Effect of
815 chronic DETA treatment on cardiac progenitor organization, represented by EGFP positive area.
816 Treatment starting at 2ss. **(G)** Representative bright-field images of human airway epithelial A549
817 cultures transfected with a non-targeting (si-Control) and *CYGB* targeting (si-Cygb) siRNAs at 0 and 24
818 hours post scratch. **(H)** Comparison of percent migration between si-Control and si-Cygb at 1.25pmol
819 and 2.5pmol. **(I)** Representative images of Western blot bands for CYGB and β-Actin. **(J)** Percent CYGB
820 protein knockdown in si-Cygb at 25pmol relative to si-Control. Student t-Test; *p<0.05; **p<0.01.

821

822 **Fig. 4. Ventricle area, ventricular diastolic volume, and stroke volume are reduced, and wall**
823 **thickness is increased in sGC mutants. (A)** Representative frames from DIC time-lapse imaging of
824 live *gucy1a1wt* and *gucy1a1*^{9bp} mutant embryos at 3 dpf showing volume at diastole and systole. Scale
825 bar, 50μM. **(B)** Schematic of ventricle position and cardiac orientation. **(C-E)** Comparison of stroke
826 volume, diastolic volume, and systolic volume between *gucy1a1wt*, and *gucy1a1*^{9bp}. **(F-H)** Comparisons
827 of stroke volume, diastolic volume, and systolic volume at 3dpf in live untreated and Bay58 treated
828 *cygb2*^{801a};Tg(*myl7*:EGFP) embryos using fluorescent time-lapse imaging, treatments starting at 2ss.
829 **(I,L)** Frames from live DIC time-lapse imaging of *gucy1a1wt*, *gucy1a1*^{9bp} , *cygb2wt* and *cygb2*^{801a}
830 mutants at 3 dpf, depicting ventricle wall thickness at diastole and systole. Scale bar, 50μM. **(L)** DETA
831 and Bay58 treatment starting at 2ss. **(J,K,M,N)** Comparison of wall thickness at diastole and systole.
832 Student t-Test; *ns*, not significant; *p<0.05; **p<0.01;***p<0.001; ****p<0.0001.

833

834 **Fig. 5. Early patterning of the anterior lateral plate mesoderm is disrupted in *cygb2* and *gucy1a1***
835 **mutants and rescued by NO–sGC activation. (A-B)** Representative in situ hybridization images (top)
836 and quantification of *drl* and *nkx2.5* expression patterns (bottom) in embryos at 10-12ss. **(A)** *drl* normal
837 expression pattern is quantified in red as percentage of embryos with distinct, short, and wide patches
838 of bilateral *drl* expression at anterior edge of ALPM. In blue, percentage of embryos with elongated
839 incongruous thin lines of bilateral *drl* expression along ALMP. **(B)** *nkx2.5* normal expression pattern is
840 quantified in red as percentage of embryos with symmetrical, uniform, and distinct bilateral *nkx2.5*
841 expression along ALMP. In blue, percentage of embryos with asymmetrical, patchy, or faint bilateral
842 *nkx2.5* expression along ALMP. Number of embryos ranked is listed within and on top of bars.
843 Treatments starting at shield. Scale bar, 200μm. On the right, schematic of ALPM anatomy with
844 embryonic orientation. Fishers exact test, ns - not significant ≥ 0.05, * P≤ 0.05, ** P≤ 0.01, *** P≤ 0.001,
845 **** P≤ 0.0001.

846

847 **Fig. 6. Disrupted specification of endothelial and myocardial lineages persists at 28 hpf and is**
848 **normalized by restoring NO–sGC signaling. (A-B)** Representative in situ hybridization images (top)
849 and quantification of *drl* and *nkx2.5* expression patterns (bottom) in embryos at 28hpf. **(A)** *drl* normal
850 expression pattern is quantified in red as percentage of embryos with expression in the anterior region
851 of the heart tube. In blue, percentage of embryos with complete loss of expression of *drl* in heart tube.
852 **(B)** *nkx2.5* normal expression pattern is quantified in red as percentage of embryos with distinct clearly
853 defined *nkx2.5* expression along the heart tube full-length. In blue, percentage of embryos with reduced
854 or absent *nkx2.5* expression in a shortened heart tube. Number of embryos ranked is listed within and
855 on top of bars. Treatments starting at shield. Scale bar, 200μm. On the right, schematic of the heart
856 tube anatomy with embryonic orientation. Fishers exact test, ns - not significant ≥ 0.05, * P≤ 0.05, **
857 P≤ 0.01, *** P≤ 0.001, **** P≤ 0.0001.